ACS Sustainable Chemistry & Engineering

pubs.acs.org/journal/ascecg

Research Article

# Metal-Free Sulfonate/Sulfate-Functionalized Carbon Nitride for Direct Conversion of Glucose to Levulinic Acid

Pawan Kumar, Ali Shayesteh Zeraati, Soumyabrata Roy, Kristen A. Miller, Aiguo Wang, Lawrence B. Alemany, Tareq A. Al-Attas, Dhwanil Trivedi, Pulickel M. Ajayan, Jinguang Hu,* and Md Golam Kibria*

Cite This: https://doi.org/10.1021/acssuschemeng.2c00309

Read Online

ACCESS | Metrics & More | Article Recommendations | Supporting Information

**ABSTRACT:** Metal-free heteroatom-doped carbonaceous materials such as carbon nitride (CN) with secondary/tertiary nitrogen-rich catalytic centers as well as chemical and thermal resilience can potentially serve as catalysts for many organic reactions. However, because of the stable alternate $Csp^2-Nsp^2$ configuration of N-linked heptazine units ($C_6N_7$), the chemical modification of CN via doping and functionalization has been a critical challenge. Herein, we report an exceptional 9.2% sulfur content in CN with sulfonate/sulfate functional groups (CNS) via a one-step in situ synthesis approach. When used as a catalyst for the dehydration/hydration of glucose, CNS catalysts demonstrate a relatively high yield and selectivity toward levulinic acid, LLA, (≈48% yield with 57% selectivity) production. CNS's high activity of direct conversion of glucose to LLA can be attributed to the synergistic catalytic effects of multiple sulfur functionalities, better dispersibility, and microstructural porosity. The synthesized CNS catalysts offer an energy efficient direct LLA production route to bypass the multistep process of sugar to LLA conversion.

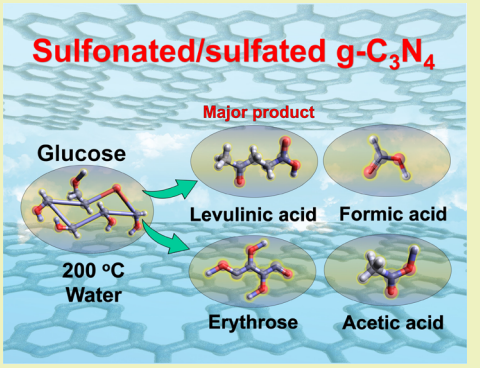


**KEYWORDS:** *carbon nitride, sulfonate/sulfate functionalization, biomass conversion, glucose dehydration, levulinic acid*



## INTRODUCTION

Biomass conversion can offer a green solution to produce chemicals and fuels from inexhaustible renewables, substituting the deleterious petroleum processes. Photosynthesis, nature's meticulous assembly, traps sunlight and $CO_2$ to transform into organic carbon of the most abundant lignocellulosic biomass (1.3 billion tons per year).[1] Cellulose constituted of $\beta(1 \rightarrow 4)$ linked D-glucose, which represents half of the organic carbon pool on the earth (annual production of $7.5 \times 10^{10}$ tons), can serve as a feedstock for the production of fuel and biodegradable chemicals.[2] Acid and enzymatic hydrolysis of cellulose to glucose are mature technologies, which can be symbiotized with chemocatalytic conversion of glucose to make platform and fine chemicals. Direct valorization of glucose to levulinic acid (LLA), which is listed in the top ten platform chemicals by the US Department of Energy (DOE),[3] is appealing for many applications. LLA has significant direct applications in pharmaceuticals, polymers, cosmetics, herbicides, pesticides, and the synthesis of chemicals such as γ-valerolactone, GVL (fuel extender, food additive), 2-methyl tetrahydrofuran (green solvent), diphenolic acid (replacing toxic bisphenol A), D-amino LLA (DALA) (pesticides), and so forth.[4−6] The global market of LLA was $186.3 million in 2020, which is expected to increase up to $379.7 million by 2026.[7]

Currently, the production of LLA at the industrial scale is achieved by using hexose (mainly glucose, fructose, and so forth) and starchy/cellulosic biomass using 1−5% mineral acids (sulfuric acid and hydrochloric acid) at 210−230 °C.[8] This process includes the removal of intermediate 5-(hydroxymethyl)furfural (HMF) followed by the recovery of LLA from the acids, which incurs extra separation processes and energy penalties, making the process expensive. To overcome the challenges with product separation, reactor corrosion,[9] homogeneous organic acids such as toluene sulfonic acid,[10] acidic ionic liquids,[11] heterogeneous metal oxide/phosphide/silicate-based solid acid catalysts, either in the pristine form[12] or functionalized with acidic groups (sulfuric/sulfonate/phosphoric/acidic −OH/COOH), have been employed for the conversion of glucose to LLA. Additionally, the use of salts such as NaCl, KCl, $CaCl_2$,[13] various solvent media such as choline chloride, or NaCl-THF/

Received: January 15, 2022
Revised: April 26, 2022

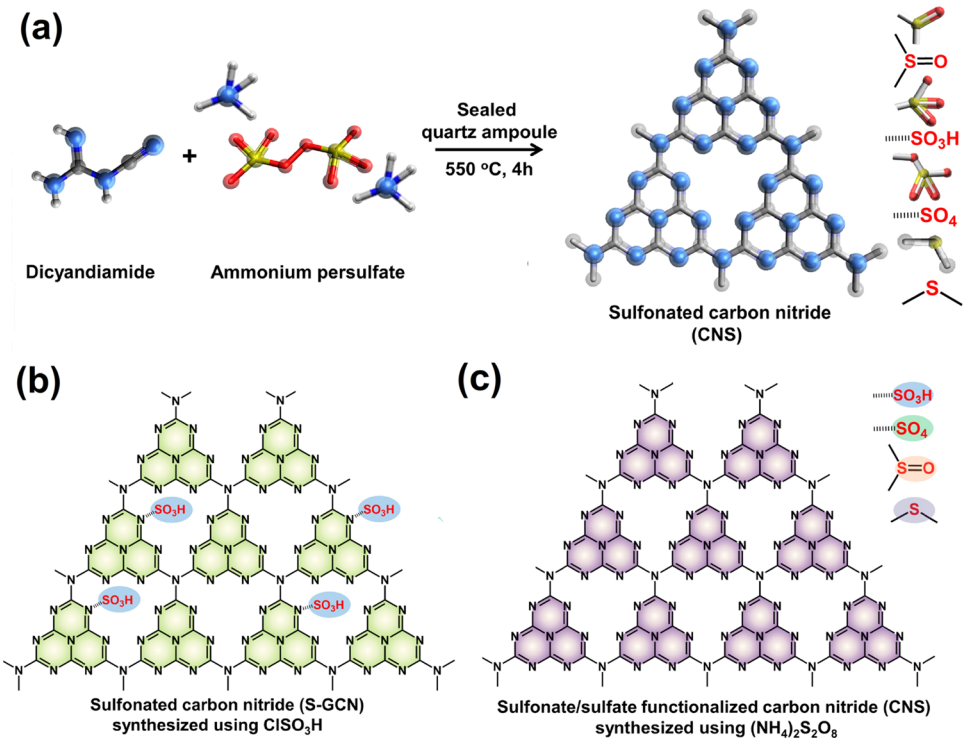


**Figure 1.** Schematic diagram of (a) solid-state synthesis of sulfonate/sulfate-functionalized S-doped CN (CNS) using dicyandiamide and ammonium persulfate in a quartz ampoule. Atoms color: C: dark gray, N: blue, O: red, S: yellow, H: white; (b) sulfonated CN (S-GCN) synthesized using $ClSO_3H$ as reported in the literature[29] and (c) CNS synthesized using ammonium persulfate in the current study.

$H_2O$ biphasic solvent[14] has also been widely explored to increase the product yield. However, the rapid deactivation of active sites, use of expensive metals, labile nature of functional groups, and contamination of reactants impede their viability at an industrial scale.

In recent years, metal-free catalysts employing doped/codoped (especially nitrogen) carbonaceous materials are gaining momentum because of their easy synthesis from earth-abundant materials, exclusion of expensive and toxic metals, high surface area, excellent thermal and chemical stability, and easy processing.[15,16] Graphitic carbon nitride (g-$C_3N_4$, CN) with intriguing physicochemical and optical properties has been widely investigated for various applications such as $CO_2$ reduction, water splitting, photo-organic transformation, and so forth.[17,18] The catalytic performance of CN arises from the primary/secondary N−H/:$NC_2$ nitrogen, face-terminated electron localization, and high surface area.[19,20] Various modification strategies such as surface area modification and functionalization have been adopted to further amplify the catalytic performance of CN. Despite the high theoretical surface area of CN, intensive stacking between the hydrogen-bonded heptazine (tris-*s*-triazine) scaffold leads to poorly exposed catalytic sites. The surface area of CN can be improved by using organic soft (Triton X-100, Pluronic P123) and inorganic hard ($SiO_2$) templates to boost the photo/catalytic performance.[21] Among functionalization strategies, the noncovalent modification of CN with various ligands/metal complexes has been extensively explored, which utilizes the electron-rich surface of CN and possible $\pi-\pi$ interactions. However, the leaching of surface-bound functionalities/metal complexes in actual reaction conditions limits their real-life applications. The covalent functionalization of CN not only offers robust binding of various molecules on the CN surface to make them recyclable but also influences charge distribution, which improves the catalytic activity in many cases.[22] For example, Gong et al. reported pyrene-functionalized CN (Py-PCN) via condensation polymerization of cyanuric chloride-modified pyrene, which displayed enhanced photocatalytic performance for the $CO_2$ reduction and cyclohexene oxidation.[23]

CN and variable valence metals/CN composites have been explored for many biomass conversion reactions, including photo/catalytic oxidation (HMF to 2,5-furandicarboxylic acid (FDCA) and 2,5-diformylfuran (DFF), fructose to DFF, furfural (FF) to maleic acid, oxidation of lignin model compounds, reduction (HMF to 2-dihydroxymethylfuran, LLA to GVL), esterification (FF to methyl furane carboxylate (MFC)), and so forth.[24−26] The applicability of CN catalysts can be further increased by functionalization with acidic sites (e.g., sulfonate group), which can promote dehydration of large sugar conjugates to employ it for complex biomass.[27,28] The existing protocol of sulfonate group functionalization of CN relies on toxic, corrosive, and expensive chlorosulfonic acid ($ClSO_3H$) in the moisture-free chlorinated solvent, dichloromethane, which restrict their scalability.[29] The limited functionalization degree and weak surface adsorption of the $-SO_3H$ group on the CN skeleton make them vulnerable to degradation over the course of the catalytic reaction. Furthermore, when employed for glucose dehydration, they usually produce furanics such as HMF, which needs an additional step for the conversion to LLA.

Here, we present a one-step approach to synthesize sulfonate/sulfate-functionalized S-doped carbon nitride (CNS) with high (~9.2 at%) sulfur content by thermal annealing of dicyandiamide and ammonium persulfate precursors in a sealed quartz ampoule (Figure 1a). We used


https://doi.org/10.1021/acssuschemeng.2c00309
ACS Sustainable Chem. Eng. XXXX, XXX, XXX−XXX

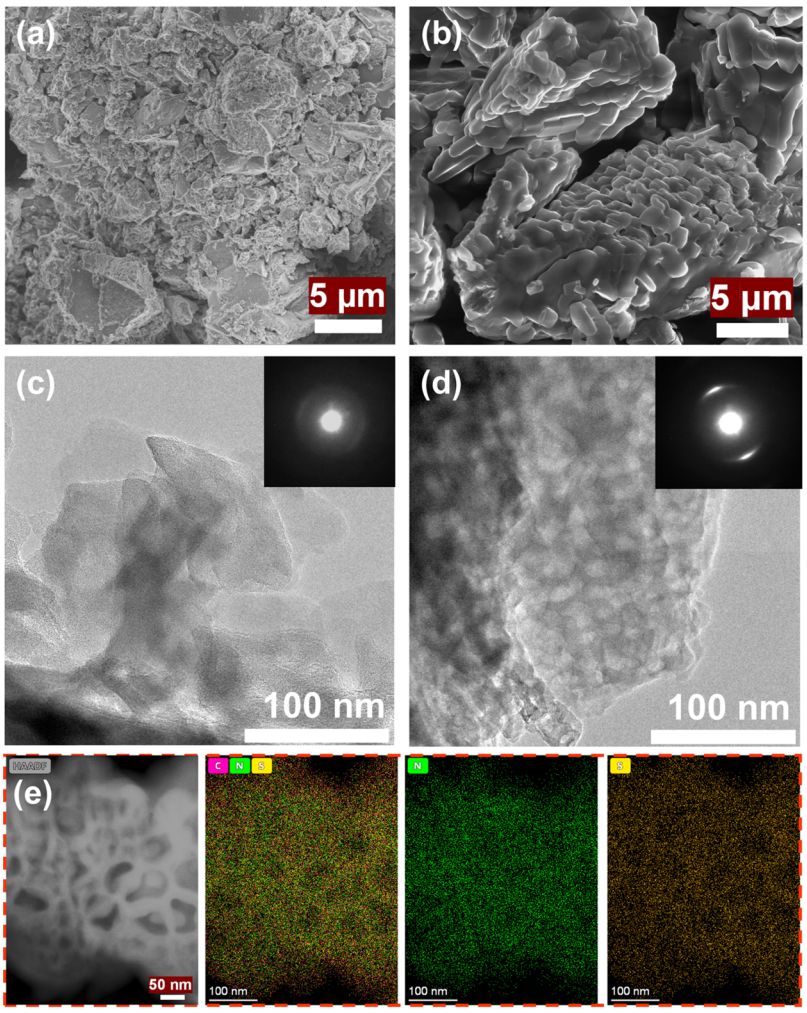


**Figure 2.** SEM images of CN (a) and CNS (b) particles; TEM images of CN (c) and CNS (d) with the corresponding SAED patterns in the figure inset. The TEM image of CNS clearly shows the porous structure; (e) HAADF-STEM image and corresponding elemental mapping for C, N, and S for a porous flakelike structure of CNS.

a low-cost precursor, that is, ammonium persulfate (APS, $(NH_4)S_2O_8$, ~$390/Mt) that disproportionates into $-SO_3$ and $-SO_4$ radicals at elevated temperatures to bond chemically with the growing polymeric CN skeleton. Sulfonated CN (S-GCN[29]) was also synthesized with $ClSO_3H$ (~$940/Mt) to compare the catalytic performance (Figure 1b,c). When used for glucose dehydration under hydrothermal conditions, CNS selectively and directly produced LLA as the main product in contrast to S-GCN, which resulted in HMF. This flipped selectivity of CNS was attributed to a high degree of chemical functionalization, increased ordered porosity, and the synergistic role of sulfate/sulfonate in CNS.

## RESULTS AND DISCUSSION

**Synthesis of CNS with a High Degree of Functionalization of Sulfonate/Sulfate.** The sulfonate/sulfate functionalized CN was synthesized by a thermal polymerization condensation reaction of dicyandiamide and ammonium persulfate in a sealed quartz tube at 550 °C (Figure 1a, Supporting Information (SI) for detailed synthesis). In this synthesis protocol, dicyandiamide works as a source of carbon and nitrogen to make an N-linked heptazine polymeric network while ammonium persulfate provides sulfur for S doping and functionalization with sulfate/sulfonate groups. The polymerization of dicyandiamide begins at about 240 °C, forming melamine followed by further polymerization to melem at 390 °C and finally CN (melon) at 525 °C.[30] Because of the low boiling point of ammonium persulfate (120 °C), the conventional synthesis protocols in the semiclosed systems hardly lead to the synthesis of S-doped/functionalized CNs. However, inside the closed quartz ampoule and pressurized system, the sulfur functionalities remain inside the reaction system and ultimately react with the polymerizing CN network, resulting in CNS. At elevated temperatures, ammonium persulfate degrades and produces the sulfate/sulfonate radical anion ($SO_4^{\bullet-}/SO_3^{\bullet-}$), which can easily react with the CN framework, resulting in sulfate and sulfonated CNS.[31−33]

It is well documented in the literature that ammonium-containing ionic liquids participate in the heptazine ($C_6N_7$) ring formation, leading to counter ion doping/functionalization in the CN scaffold.[34,35] Previous reports on the synthesis of triazine ($C_3N_3$)-based graphitic CN (TGCN) and heptazine ($C_6N_7$)-based CN using ampoule synthesis and molten salts suggest that a closed system with a high temperature and pressure improve the crystallinity/periodicity of the CNs, giving rise to better electronic properties.[36,37] To know the optimum precursor concentration, four CNS samples with 5,


https://doi.org/10.1021/acssuschemeng.2c00309
ACS Sustainable Chem. Eng. XXXX, XXX, XXX−XXX

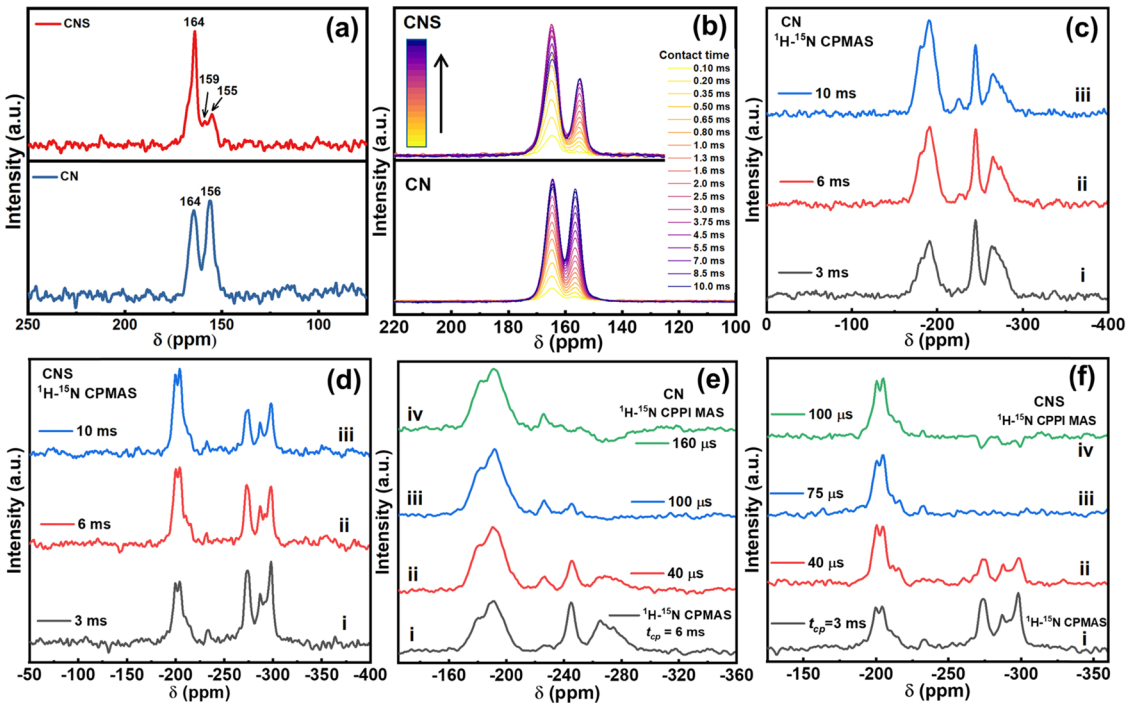


**Figure 3.** (a) Direct excitation 50.33 MHz $^{13}C$ ssNMR spectra of CN and CNS (b) evolution of $^{13}C$ NMR signals with different contact times for CN and CNS (c) 20.28 MHz $^{1}H$-$^{15}N$ CPMAS spectra of pristine CN obtained under the same conditions except for different contact times: (i) $t_{cp}$ = 3 ms, (ii) $t_{cp}$ = 6 ms, and (iii) $t_{cp}$ = 10 ms. The spectra are plotted with the same level of baseline noise to facilitate comparison. (d) 20.28 MHz $^{1}H$-$^{15}N$ CPMAS spectra of CNS obtained under the same conditions except for different contact times: (i) $t_{cp}$ = 3 ms, (ii) $t_{cp}$ = 6 ms, (iii) $t_{cp}$ = 10 ms. The spectra are plotted with the same level of baseline noise to facilitate comparison. (e) (i) 20.28 MHz $^{1}H$-$^{15}N$ CPMAS spectrum of pristine CN obtained with a contact time $t_{cp}$ = 6 ms. 20.28 MHz $^{1}H$-$^{15}N$ CPPI MAS spectra of CN obtained with $t_{cp}$ = 6 ms and a subsequent polarization inversion time $t_i$ of (ii) 40 $\mu$s, (iii) 100 $\mu$s, (iv) 160 $\mu$s. (f) (i) 20.28 MHz $^{1}H$-$^{15}N$ CPMAS spectrum of CNS obtained with a contact time $t_{cp}$ = 3 ms. $^{1}H$-$^{15}N$ CPPI MAS spectra (20.28 MHz) of CNS obtained with $t_{cp}$ = 3 ms and a subsequent polarization inversion time $t_i$ of (ii) 40 $\mu$s, (iii) 75 $\mu$s, (iv) 100 $\mu$s.

10, 15, and 20 wt % of ammonium persulfate with respect to dicyandiamide were synthesized and denoted as CNS-5, CNS-10, CNS-15, and CNS-20, respectively. In the following sections, the acronym CNS would refer to sample CNS-15. Furthermore, for comparison, pristine CN (CN) was also synthesized by thermal annealing of dicyandiamide at 550 °C.

**Catalyst Characterization.** The morphological characteristics of the samples were determined using field emission scanning electron microscopy (FESEM). The SEM image of bulk CN shows an agglomerated sheet structure (Figure 2a). At relatively high magnifications, the crumpled sheet structure is more apparent, suggesting well-constituted CN sheets (Figure S1). As expected, the energy-dispersive X-ray spectroscopy (EDS) mapping of the CN shows the presence of well-distributed C, N, and O substantiating the C−N scaffold with residual oxygen functionalities/adsorbed water (Figure S1d−g). Interestingly, the SEM image of CNS shows a nanocolumnar structure, which might be due to the formation of the relatively more crystalline structure under self-pressurized conditions (Figure 2b). The EDS elemental mapping of the samples shows uniform distribution of C, N, O, and S elements corroborating the presence of S-functionalities throughout the sample (Figure S2d−h).

The HRTEM image of CN (Figure 2c) shows a crumpled graphitic sheet structure with morphology that can be attributed to the formation of the H-bonded bulk structure during the $NH_3$ evolution in the polymerization reaction. The selected area electron diffraction (SAED) pattern of CN does not show any sharp spots/rings demonstrating its amorphous nature. Interestingly, the TEM images of CNS show an intriguing porous graphitic structure (Figures 2d and S3). The polymerization of dicyandiamide proceeds with the evolution of $NH_3$ gas, while at the same time, ammonium persulfate also disproportionates, and the resulting gaseous mixture gives rise to a porous structure. The SAED pattern of CNS shows some diffraction spots, which might be due to increased crystallinity of the materials in closed system solid-state synthesis (inset of Figure 2d). Furthermore, STEM elemental mapping (Figure 2e) displays a uniform distribution of each constituting element (C, N, and S) in the material.

Solid-state $^{13}C$ and $^{15}N$ NMR studies were performed on CN and CNS to obtain additional information. Direct $^{13}C$ pulse, MAS spectra are shown in Figure 3a. Pristine CN exhibits signals of nearly equal intensity at 156 and 164 ppm. The relative signal intensities are meaningful, as they remain the same within experimental error when the relaxation delay is lengthened from 10 to 30 s. The signal at 156 ppm can confidently be attributed to the three bridgehead $CN_3$ carbons of the heptazine units ($C_6N_7$), and the signal at 164 ppm can confidently be attributed to the three carbons bonded to the NH groups connecting heptazine units based on calculations[38,39] and the relative rate of cross-polarization of the two signals in a separate series of experiments with different contact times.[40,41] The same assignments have been reported for other samples of CN.[42,43]

For our sample of pristine CN, the signal at 164 ppm cross-polarizes significantly faster than the signal at 156 ppm, consistent with stronger $^{1}H$-$^{13}C$ dipole−dipole interactions for


https://doi.org/10.1021/acssuschemeng.2c00309
ACS Sustainable Chem. Eng. XXXX, XXX, XXX−XXX

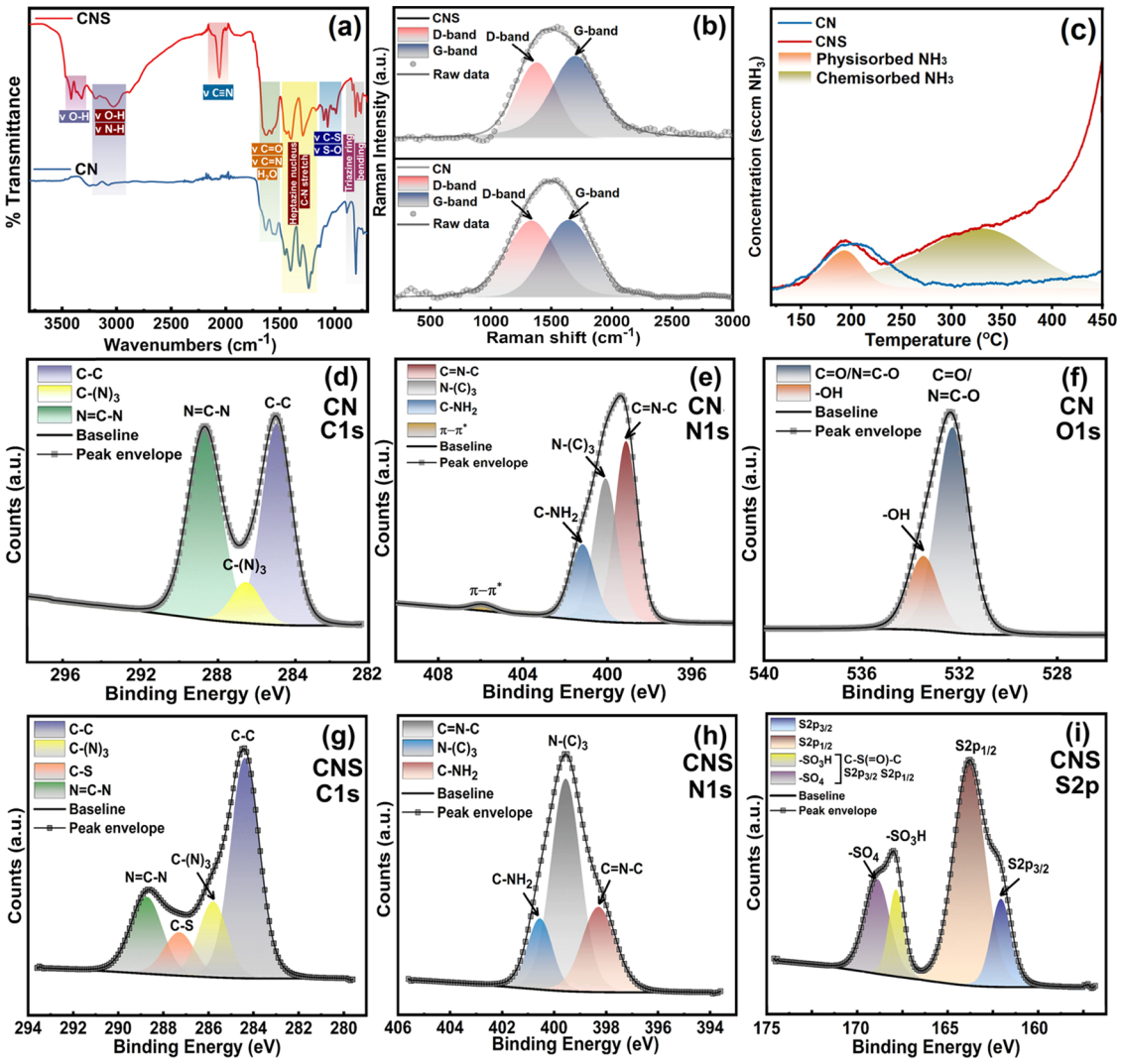


**Figure 4.** (a) FT-IR spectra of CN and CNS; (b) Raman spectra of CN and CNS showing specific D and G bands for the graphenic structure; (c) $NH_3$-TPD spectra of CN and CNS; only the CNS peak is deconvoluted for simplicity. Component peak fitting of XPS spectra of the synthesized CN (d–f) and CNS (g–i): (d and g) C 1s region, (e and h) N 1s region, (f) O 1s region of CN, and (i) S 2p region of CNS.

the carbons bonded to the NH groups resulting from closer proximity to protons. Specifically, in a multiple contact time experiment with 18 contact times ranging from 0.1 to 10.0 ms, the intensity of the signal at 164 ppm reaches a maximum at a contact time of 4.5−5.5 ms, while the intensity of the signal at 156 ppm is still increasing at a contact time of 10.0 ms (Figure 3b). These observations closely parallel those for model $C_6N_7(NH_2)_3$ (melem).[40] Even with a contact time of just 0.2 ms, the S/N for the weaker signal at 156 ppm is comparable to the S/N in the direct $^{13}C$ pulse experiment obtained with a 30 s relaxation delay in experiments taking 3.4 and 52.8 h, respectively. The CP experiment with a contact time of 10.0 ms provides relative signal intensities that come closest to those obtained in the direct $^{13}C$ pulse spectrum (Figure 3a) only because $^{1}H$ spin−lattice relaxation in the rotating frame reduces the intensity of the signal at 164 ppm while the intensity of the signal at 156 ppm continues to increase. Previous work has shown that the $^{13}C$ nuclei of CN relax very slowly.[42]

The direct $^{13}C$ pulse spectrum of CNS clearly differs from that for pristine CN. The signal for the bridgehead $CN_3$ carbons (155 ppm) is noticeably weaker than the more downfield signal (165 ppm) in spectra obtained with a 10 or 30 s relaxation delay. The two signals cross-polarize at very different rates, just as with pristine CN. The intensity of the more downfield signal (165 ppm) in CNS reaches a maximum at a contact time of 2.0−3.0 ms; the intensity of the more upfield signal (155 ppm) reaches a maximum at a contact time of 7.0−10.0 ms (Figure 3b). Again, even with a contact time of just 0.2 ms, the S/N for the weaker signal at 156 ppm is comparable to the S/N in the direct $^{13}C$ pulse experiment obtained with a 30 s relaxation delay in experiments taking 2.7 and 64.0 h, respectively. The CP experiments with short contact times (up to about 0.8 ms) provide relative signal intensities that come closest to those obtained in the direct $^{13}C$ pulse spectrum (Figure 3a).

The spectroscopic differences compared to pristine CN are readily apparent. We believe that the most likely explanation is the incorporation of sulfur, instead of nitrogen, into the heptazine framework during its formation, resulting in a C−S−C group instead of a C═N−C group. Support for the presence of a C−S−C group comes from the strong S 2p signal in the XPS spectrum at 163.6 eV (Figure 4i).[44−48] The shoulder on the signal can be attributed to the signal resulting from the


https://doi.org/10.1021/acssuschemeng.2c00309
ACS Sustainable Chem. Eng. XXXX, XXX, XXX−XXX

superposition of the S $2p_{3/2}$ and S $2p_{1/2}$ components.[48] The absence of quaternary aliphatic carbon signals in the spectrum of CNS is noteworthy because such carbons would be generated if $-SO_3H$ or $-OSO_3H$ groups were added to framework carbon. There is the possibility of the aliphatic $^{13}C$ signal being severely broadened by being bonded to three (quadrupolar) $^{14}N$ nuclei and one $^{32}S$ nucleus, although it is clear that the aromatic $^{13}C$ signal for either type of carbon bonded to three $^{14}N$ nuclei in pristine CN can be detected.

MAS $^{15}N$ NMR has been extensively used to characterize various forms of CN before and after functionalization[42,43,49−56] as well as precursors such as melamine,[38,57,58] functionalized melamine,[59] melam,[58] melem,[38,40,58] functionalized melem,[60−63] other heptazine structures,[64−66] melon,[39,41] and functionalized melon.[67] The $^{15}N$ chemical shift assignments in many of these reports facilitate analyzing the spectra of our samples of pristine CN and sulfurized CNS. Because $^{15}N$ is a low abundance nucleus (0.37%) of low sensitivity ($3.85 \times 10^{-6}$ relative to $^{1}H$ at natural abundance), $^{15}N$-enriched reagents were used in some of the previous studies,[38−42,49−51,54,55,59,67] while the extraordinarily sensitive DNP MAS technique was used in another.[43]

Pristine CN and CNS were initially studied by $^{1}H$-$^{15}N$ CPMAS with contact times ($t_{cp}$) of 3, 6, and 10 ms in order to get at least qualitative information on the relative rates of cross-polarization of the different types of nitrogen environments. These spectra are shown in Figure 3c (CN) and Figure 3d (CNS). Sulfurization has an obvious effect. The signals in the $^{1}H$-$^{15}N$ CPMAS spectra of CN can reasonably be assigned in light of prior work. The most downfield signals (from about −170 to −210 ppm) can reasonably be assigned to C═N−C on the periphery of a condensed ring system. These signals become proportionately stronger as the contact time is lengthened. The weak signal at −226 ppm can reasonably be assigned to the interior $NC_3$ of a melem-type environment. Because this nitrogen is relatively far from protons, it cross-polarizes much more slowly. The signal is not visible above the noise with a contact time of 3 ms. The signal is barely detectable with a contact time of 6 ms. The signal is clearly above the noise with a contact time of 10 ms. The signal at −245 ppm can reasonably be assigned to NH groups bridging two condensed ring systems. The most upfield signals (from about −260 to −290 ppm) can reasonably be assigned to $NH_2$ groups attached to condensed ring systems.

The $^{1}H$-$^{15}N$ cross-polarization, polarization inversion (CPPI) experiment[38,39,51,58−60,64,65,68−70] provides strong support for these assignments. In this experiment, the polarization inversion period $t_i$ following the traditional cross-polarization period $t_{cp}$ allows the $^{15}N$ signals to decay through $^{1}H$-$^{15}N$ dipole−dipole coupling. A value of $t_{cp}$ is chosen to try to maximize the $^{15}N$ signal intensity. The phase of either the $^{1}H$ or $^{15}N$ spin locking rf field is then shifted by 180° during the $t_i$ period to allow magnetization decay. In general, $^{15}NH_2$ signals decay the most quickly; $^{15}NH$ signals decay somewhat more slowly, and signals from fully substituted $^{15}N$ nuclei decay much more slowly. Potential complications arise from variations in molecular motions and in the local proton environment (e.g., variations in hydrogen bonding in nominally the same nitrogen environment).[68,69,71] Previous studies on $^{15}N$-enriched melamine and melem,[38] functionalized melamine,[59] a melamine-melem adduct and a melam-$ZnCl_2$ complex,[58] $^{15}N$-enriched C/N/H-graphite,[39] and a heptazine structure[65] facilitated estimating $t_i$ values to use in setting up a series of experiments to differentiate $^{15}NH_2$ signals from $^{15}NH$ signals in the CN and CNS samples.

Figure 3e shows the standard $^{1}H$-$^{15}N$ CPMAS spectrum of CN obtained with a contact time $t_{cp}$ = 6 ms and the CPPI MAS spectra obtained with the same contact time and subsequent polarization inversion periods $t_i$ of 40, 100, and 160 μs. The CPPI spectra confirm the assignments above. The signals upfield of −255 ppm rapidly become weaker ($t_i$ = 40 μs), become just slightly inverted ($t_i$ = 100 μs), and become much more inverted ($t_i$ = 160 μs), consistent with $^{15}NH_2$. The relatively sharp signal at −245 ppm more slowly decreases in intensity, exhibiting a null at $t_i$ = 160 μs, consistent with $^{15}NH$. The weak signal at −226 ppm and the band of signals from about −170 to −210 ppm much more slowly decrease in intensity, consistent with fully substituted $^{15}N$. The rates of signal decay for $^{15}NH_2$, $^{15}NH$, and fully substituted $^{15}N$ are completely consistent with those observed for a tricyanomelaminate,[59] a melam-$ZnCl_2$ complex,[58] and a C/N/H-graphite.[39] The $^{1}H$-$^{15}N$ CPMAS spectra of CNS (**CNS**, Figure 3d clearly differ from those of pristine CN obtained with the same contact time (Figure 3c). The differences are much greater than those in a comparison of the corresponding $^{1}H$-$^{13}C$ cross polarization spectra and thus demonstrate the utility of $^{15}N$ NMR.

As with sample CN, the CNS signals downfield of −220 ppm can be assigned to C═N−C on the periphery of a condensed ring system and become proportionately stronger as the contact time is lengthened. The weak signal at −232 ppm can again reasonably be assigned to the interior $NC_3$ of a melem-type environment. However, it is not obvious if the CNS signals from about −270 to −305 ppm result only from $NH_2$ environments, as the presence of any unusually shielded bridging NH groups after sulfur treatment could not be ruled out. (For reference, the NH groups in the two crystallographically independent melam molecules exhibit NH signals at −252.0 and −254.8 ppm;[58] the NH group in a melam-$ZnCl_2$ complex exhibits a signal at −254 ppm;[58] and the NH group in a C/N/H-graphite exhibits a signal at −245 ppm.[39]) However, the CPPI MAS spectra of CNS obtained with a contact time $t_{cp}$ = 3 ms and subsequent polarization inversion periods $t_i$ of 40, 75, and 100 μs lead us to believe that all of the signals upfield of about −270 ppm result from $^{15}NH_2$ environments, as these signals rapidly weaken ($t_i$ = 40 μs), null ($t_i$ = 75 μs), and invert ($t_i$ = 100 μs) at very similar rates (Figure 3f). The signals null even faster (at $t_i$ = 75 μs) than do the corresponding signals for the $^{15}NH_2$ groups in CN ($t_i$ = 100 μs). For NH groups to be present in CNS and null at $t_i$ = 75 μs, they would have to be in very rigid environments, resulting in uncommonly strong $^{1}H$-$^{15}N$ dipole−dipole interactions. However, it is not obvious how the incorporation of sulfur instead of nitrogen into the heptazine framework during its formation, that is, the formation of C−S−C groups instead of C═N−C groups, would result in very rigid and unusually shielded environments for the NH groups of CNS. Thus, sulfur treatment apparently cleaves a C−N bond of the bridging NH group for all Ar-NH-Ar units in pristine CN (where Ar = condensed heteroaromatic ring system), resulting in much smaller molecular entities in CNS. In light of prior work,[39,42,66,67] the long $^{15}N$ spin−lattice relaxation times $T_1$ that would be expected for CN and CNS, particularly for ring nitrogens, preclude using direct $^{15}N$ pulse experiments with these natural abundance materials to try to determine the relative amounts of the different nitrogen environments present in CN and CNS. In general, significant


https://doi.org/10.1021/acssuschemeng.2c00309
ACS Sustainable Chem. Eng. XXXX, XXX, XXX−XXX

differences in the $^{1}H$-$^{15}N$ cross-polarization rates $T_{NH}$ among the different types of nitrogens and significant differences in the $^{15}N$ spin−lattice relaxation rates $R_1$ among the different types of nitrogens make it difficult to accurately determine the relative amounts of the different nitrogen environments in CN-type materials.

The infrared-active vibrational features specific to the functional groups and N-linked heptazine ring structure of CN and CNS were identified using Fourier transform infrared spectroscopy (FT-IR) (Figure 4a). The FT-IR spectra of pristine CN exhibits an intense peak at 806 $cm^{-1}$ specific to the triazine ($C_3N_3$) ring bending vibration of the heptazine ($C_6N_7$) moiety.[72] The FT-IR bands extending from 1163−1460 $cm^{-1}$ have arisen from the cumulative symmetric and asymmetric C−N stretching vibrations of the heptazine ($C_6N_7$) nucleus.[73] The FT-IR signals at 1554 $cm^{-1}$ are originated from the C═N ($\nu_{C=N}$) stretching and $H_2O$ ($\delta_{H2O}$) bending vibrations while another peak at 1632 $cm^{-1}$ is ascribed to the C═O ($\nu_{C=O}$) stretching vibration of the terminal uncondensed functionalities and surface-adsorbed water molecules.[74] The vibrational bands with some splitting ranging from 3050 to 3320 $cm^{-1}$ in the FT-IR spectra of CN appeared from the combinational vibration of terminal uncondensed $-NH_2$/NH ($\nu_{N-H}$) and −OH ($\nu_{O-H}$) stretching vibrations of residual oxygen-carrying functionalities and adsorbed water.[75] The vibrational spectra of CNS display all the signature stretching/bending vibrations of the N-linked $C_6N_7$ long-range order structure corroborating the presence of an intact CN network. Additionally, because of S doping and sulfonate/sulfate functionalization on the CN network, some new peaks also appeared. The new FT-IR peaks ranging from 982−1124 $cm^{-1}$ originated from the C−S and S−O stretching vibrations of C-linked sulfonate/sulfate groups.[76,77] An intense peak at the 2065 $cm^{-1}$ appeared due to uncondensed −C≡N groups from the dicyandiamide precursor.[78] Because of the restricted vibrational degree of freedom, the C≡N stretching vibration appeared much sharper than the other peaks.[79] Furthermore, in addition to the vibrational stretch of the uncondensed $-NH_2$/NH ($\nu_{N-H}$) and −OH ($\nu_{O-H}$), additional peaks at the higher frequency (3328−3430 $cm^{-1}$) are attributed to chemically functionalized −OH stretching of sulfonate ($-SO_2$-OH) and sulfates ($SO_3$-OH).[80] The functionalization can further be confirmed with Raman and X-ray diffraction analyses (Figures 4b, S4, and Section 4.0 of the Supporting Information). It is worth mentioning that CNS showed enhanced dispersibility in water compared to CN, which might be due to the presence of plenty of hydrophilic sulfonate/sulfate functionalities and relatively small fragments of the heptazine network as evidenced by NMR. This is indirect evidence of the surface functionalization of CN. To probe the better dispersibility due to sulfonate/sulfate functionalization, the sample surface charge was determined calculating apparent zeta potential ($\zeta$) particle size distribution (Section 4.3, Figure S5−S7 in the Supporting Information) The zeta potential of CNS was found to be −38.1 mV, which was much higher than CN (−29.1 mV) suggesting the presence of polar functionalities on the surface of CNS.

To validate the presence of acidic sulfonate ($-SO_2$-OH) and sulfate ($SO_3$-OH) sites, ammonia temperature-programmed desorption ($NH_3$-TPD) analysis was performed on CN and CNS samples (Figure 4). The $NH_3$-TPD of CN displayed a small desorption peak around 190 °C because of the release of physiosorbed $NH_3$. No other desorption peak was observed to substantiate the absence of any acidic sites and complied with plenty of Bronsted/Lewis base sites on the CN scaffold.[81] CNS also displayed a physisorption peak of almost equal strength at 190 °C, indicating a similar heptazine constituted network. However, after 270 °C, strong desorption of $NH_3$ was observed to be extended up to 450 °C. Similar desorption profiles have been previously reported for acidic sites containing CNs.[82] Noteworthy, the desorption profile of CNS was significantly different than sulfonated SGCN, which displayed distinct $NH_3$ desorption in between 200−350 °C (centered at 270 °C).[29,83] Compared to SGCN where sulfonic acid groups were physisorbed on CN scaffold, the CNS contains chemically bound $-SO_3H/SO_4$ groups, resulting in the observance of TPD signals at a relatively higher temperature. Furthermore, the distinction between $-SO_3H/SO_4$ desorption signals was not possible, probably due to the almost identical chemical nature, resulting in $NH_3$ desorption in the same temperature range. Peak deconvolution shows maximum desorption around 325 °C, and after that, sharp $NH_3$ desorption was observed. As CNS has smaller fragments with relativity freer $NH/NH_2$, the sharp changes might be due to the evolution of $NH_3$ during the condensation of residual amino functionalities. The thermal stability and nature of surface chemical functionalities were also determined using thermogravimetric analysis (TGA)−differential scanning calorimetry (DSC), which demonstrate weight loss corresponding to the degradation of sulfonate/sulfate moieties (Section 4.4, Figure S8 in the Supporting Information).

The XPS elemental survey scan of CN exhibits all the core-level peaks corresponding to C, N, and O elements (Figure S9a). The high-resolution XPS spectra of CN in the C 1s and N 1s regions show all signature peaks associated with tertiary ($C-(N)_3$), secondary (N−C═N) carbons and $sp^2$-hybridized secondary N's (C═N−C), tertiary nitrogens ($N-(C)_3$), and uncondensed/hydrogen-bonded terminal nitrogens ($-NH_2$/NH) (Figure 4d,e).[84,85] A weak signal around 405.9 eV can be ascribed to the $\pi-\pi^*$ electronic transitions in the $sp^2$ N-linked CN skeleton.[86] The O 1s HR-XPS of CN in the O1s region was deconvoluted in two peak components with a BE shift of 532.3 and 533.5 eV assigned to C═O/N═C−O and surface-adsorbed water and adventitious −OH oxygens (Figure 4f).[87]

Similarly, the elemental XPS survey scan of CNS exhibits all the core-level peaks of C, N, and O along with additional peaks of S (S 2s and S 2p, etc.), demonstrating the integration of S doping/functionalities in the $C(sp^2)-N(sp^2)$ core structure of CN (Figure S9b). The reaction of ammonium persulfate with polymerizing dicyandiamide at elevated temperatures under pressure in a closed system leads to an exceptionally high sulfur doping/functionalization (S content: 9.2 at%). To the best of our knowledge, such a high amount of S-doping and functionalization in the CN structure has not yet been reported in the literature. The HR-XPS spectra of CNS in the C 1s region show four peaks (Figure 4g). The peak centered at 284.6, 285.8, and 288.7 eV can be assigned to the adventitious $sp^3$ C, $sp^2$-hybridized tertiary ($C-(N)_3$), and secondary (N−C═N) carbons, respectively. Additionally, a new peak centered at 287.5 eV also appeared because of the presence of C−S type of carbons in the CN network.[88−90] The CNS structure shows a relatively high C−C peak intensity compared to CN, which might be due to the partial condensation and introduction of sulfonates/sulfates. The three peak components in the N 1s XPS of CNS positioned at 398.3, 399.6, and 400.6 eV are assigned to $sp^2$-hybridized


https://doi.org/10.1021/acssuschemeng.2c00309
ACS Sustainable Chem. Eng. XXXX, XXX, XXX−XXX

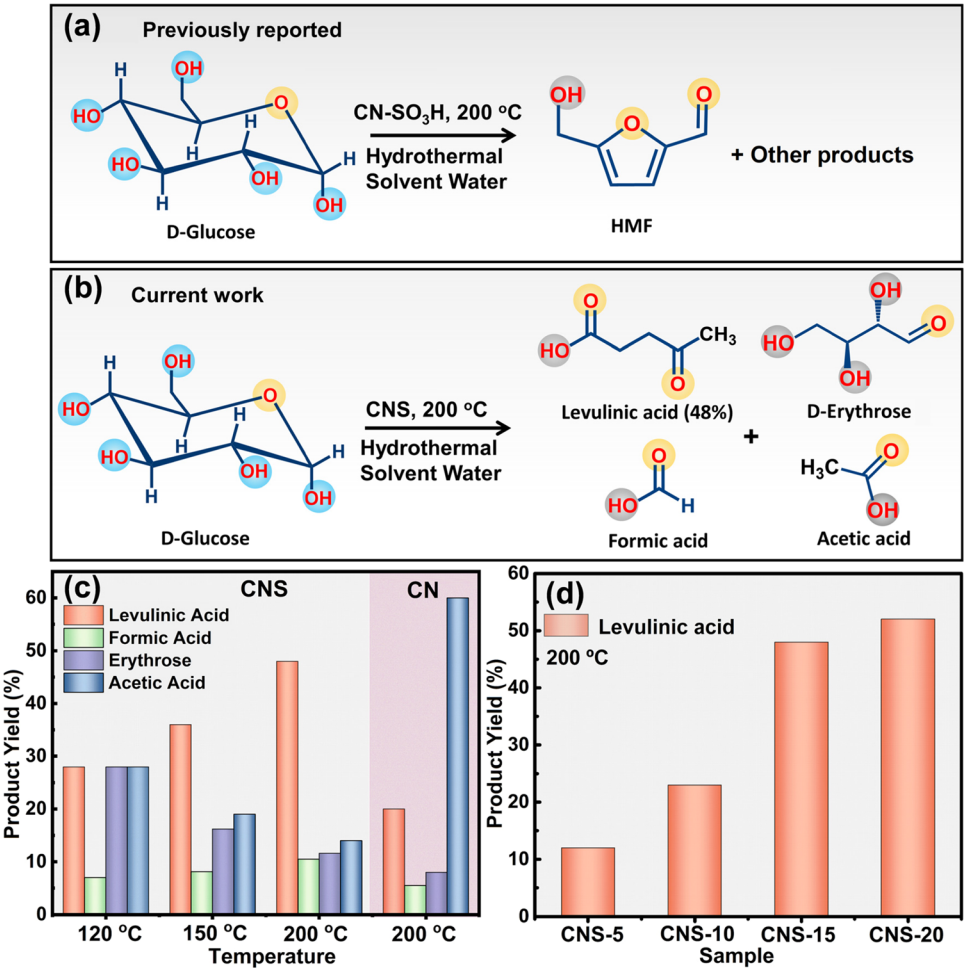


**Figure 5.** Schematic diagram showing the product selectivity using previously reported (a) S-GCN (CN-$SO_3H$) and (b) CNS catalysts; (c) product distribution of glucose hydrothermal oxidation as a function of temperature using CNS and CN. (d) LLA yield using CNS-5, CNS-10, CNS-15, and CNS-20 samples synthesized by 5−20 wt % of ammonium persulfate. (Reaction conditions: glucose = 0.1 g, catalyst = 10 mg, DI water = 10 mL for 4 h).

secondary N's (C═N−C), tertiary (N−$(C)_3$), and primary $sp^3$ nitrogens (Figure 4h), respectively.[91] Interestingly, for CNS, the peak intensity of secondary (C═N−C) N's decreased, which might be due to the functionalization of peripheral C═N−C with the $-SO_3/SO_4$ groups.[92,93] Furthermore, the $\pi-\pi^*$ transition peak was almost disappeared for the CNS, suggesting a reduced conjugation degree due to the functionalization. The S 2p XPS spectra of CNS show two major peaks, which can be further deconvoluted into four peak components (Figure 4i). The intense peak centered at 163.6 eV associated with a weak shoulder peak at 161.9 eV originated from the S $2p_{1/2}$ and S $2p_{3/2}$ components of S atoms doped inside the heptazine ($C_6N_7$) nucleus by replacing N atoms (C−S−C).[38−42] Calculations by others[36,39] indicate that replacement of N by S on the periphery of the heptazine framework appears to be energetically more favorable than the replacement of the central N bonded to three C. Replacement of the central N would result in a positively charged, three-coordinate sulfur environment. The doping of S atoms inside the heptazine units was also evident from the increased visible absorption and uplifted valence band positions (Figure S11−12). The peak positioned at 167.7 eV of the S 2p XPS spectra of CNS can be ascribed to the presence of sulfur in the form of $-SO_3$ (sulfonate), while the second peak component centered at 168.86 eV is assigned to $-SO_4$ (sulfate) groups bonded to the heptazine structure.[94] Because doping of the S atom in the heptazine unit by the replacement of N is not isoelectronic, it will also lead to the oxidation of C−S−C moieties to a sulfoxide C−S(═O)−C. The XPS S 2p signal for C−S(═O)−C has been reported at 168.0 eV, resulting from the overlap of the S $2p_{1/2}$ and S $2p_{3/2}$ components.[48] It should be noted that the carbons in the resulting C−S(═O)−C group would still be aromatic. Because the peak components at 168.9 and 167.7 eV is originated from the combinational contribution of $-SO_3H/SO_4$ and S $2p_{1/2}$ and S $2p_{3/2}$ components of C−S(═O)−C, the exact quantification of $-SO_3H/SO_4$ is not possible.[25,53] The relative at% ratio of $-SO_3/-SO_4$ or C−S(═O)−C S $2p_{3/2}$/S $2p_{1/2}$ was calculated to be 35/65, demonstrating a significant amount of sulfate moieties in the structure. It is worthy to mention here that $SO_3/SO_4$ peak components were not further deconvoluted into $2p_{3/2}$ and $2p_{1/2}$ peak components because the exact contribution of C−S(═O)−C and $SO_3/SO_4$ groups cannot be determined. Two peak components in the O 1s spectra of CNS at 531.4 and 532.5 eV are assigned to oxygen atoms present in $-SO_3/SO_4$ groups (S is less electronegative than N) and residual/adventitious N═C−O/C═O/−OH groups (Figure S10).[95]


https://doi.org/10.1021/acssuschemeng.2c00309
ACS Sustainable Chem. Eng. XXXX, XXX, XXX−XXX

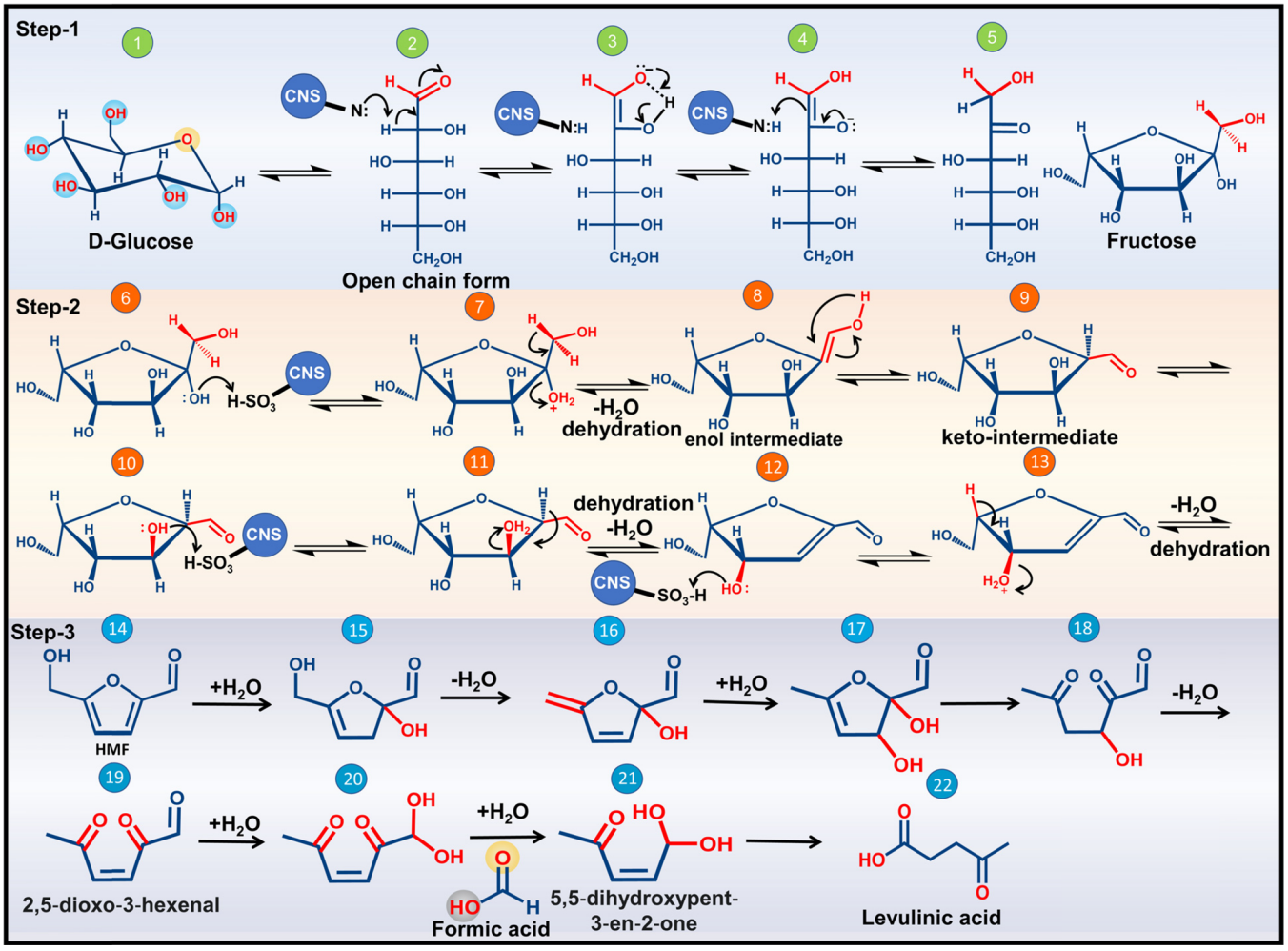


**Figure 6.** A plausible mechanism of glucose dehydration to LLA.

Analyzing the structure of CNS by various techniques indicates that multiple forms of sulfur are incorporated: sulfide (C−S−C), sulfoxide [C−S(=O)−C], sulfonate ($SO_3H$), and sulfate ($SO_4H$). However, the replacement of N by S in the heptazine CN scaffold is not isoelectronic and therefore requires structural modification (e.g., radicals in two fragments combining through the formation of a new single bond). Furthermore, functionalizing C in the scaffold with sulfonate or sulfate would generate a quaternary aliphatic carbon bonded to S (sulfonate) or O (sulfate) and three N, but there do not appear to be any readily available model compounds with such environments to use as reference materials for the characterization of CNS by IR, XPS, and NMR. Additional work will be required before trying to propose a structure of CNS consistent with all of the analytical results.

**Catalytic Performance.** The catalytic performance of synthesized materials was evaluated for hydrothermal dehydration of glucose. Previous studies on the modification of the CN structure using chlorosulfonic acid ($ClSO_3H$, to form sulfonated CN) suggest that the presence of plenty of acidic sites promotes the dehydration of glucose to furanics.[28,29] Beyond glucose conversion, sulfonated CNs (S-GCN) also promote the dehydration of other monosaccharides such as xylose and fructose to furanics (i.e., HMF) (Figure 5a)[28] and transesterification of fatty acid to form biodiesel conjugates.[27] Interestingly, in our study, LLA was observed as the dominant product when CNS was used as a catalyst for glucose dehydration (Figure 5b). This was supplemented with formic acid (FA), erythrose, and acetic acid (AA) as minor products. The reaction was run at different temperatures (120, 150, and 200 °C) to investigate its impact on product selectivity (Figure 5c and Table S1). At lower temperatures (120 °C), the selectivity of LLA was only 28%. As the bond breaking of C6 glucose to LLA (C5) proceeds via the elimination of FA, an equal concentration of FA (C1) in the reaction product was expected. However, the FA selectivity in the reaction mixture was found only 7%. This low yield of FA can be due to further oxidation of formic acid to $CO_2$ and water under catalytic hydrothermal conditions.[96,97] Another major product observed at 120 °C was erythrose (C4 sugar) which forms via the elimination of AA (C2). The relative yield of the erythrose and acetic acid was calculated to be 28% for each component. The presence of C4 erythrose and C2 acetic acid in equal amounts strengthens the formation of these products via glucose bond cleavage at the C2 position.[98] As the temperature of the reaction was raised to 150 °C, the LLA selectivity was raised to 36% along with a slight increment of FA yield from 7 to 8.1%. The yield of erythrose and AA decreased to 16.5 and 19.0%, respectively. The optimum temperature for glucose dehydration to LLA was found to be 200 °C, leading to an LLA yield of about 48%. At 200 °C FA, erythrose and AA were found to be 10.5, 11.6 and 14.0%, respectively. In all the reactions, ~4−


https://doi.org/10.1021/acssuschemeng.2c00309
ACS Sustainable Chem. Eng. XXXX, XXX, XXX−XXX

5% lactic acid with a trace of fructose were also observed, which suggest that the dehydration of glucose proceeds through isomerization of glucose to fructose with the subsequent formation of lactic acid as a side product via retro-aldol reaction.[99] No glucose was observed in the reaction products, indicating 100% conversion of glucose. However, this 100% conversion cannot be directly correlated to product yield because a significant fraction in the hydrothermal process gets transformed to humus (a polymerization product of furanics).[100]

To validate that the sulfate/sulfonate functionalization of CNS is the active catalyst, we have run control experiments using CN as a catalyst under identical conditions (200 °C), which only exhibited ∼20% yield for the LLA. Interestingly, pristine CN alone gives a significantly high AA yield reaching up to 60%, suggesting a different reaction mechanism by sulfate/sulfonate functional groups. Using CNS as a catalyst, the LLA yield was almost 2.5 times higher than that of CN. Furthermore, sulfonated CN (S-GCN)[27,29] was also prepared and tested for glucose hydration, which yielded HMF as a major product with a small amount of erythrose and acetic acids (Figure 5a and Table S2). The CNS catalysts were also tested for the fructose conversion to LLA, which yielded 35% LLA, demonstrating that the scope of these catalysts is applicable for different monomer sugars (Table S2). The reaction without any catalyst at 200 °C does not give any significant product.

Furthermore, the effect of ammonium persulfate precursor concentration on the LLA yield was studied. The CNS catalysts, CNS-5, CNS-10, CNS-15, and CNS-20, were tested toward hydrothermal glucose dehydration at 200 °C (Figure 5d). The CNS-5 gave 12% of LLA, while for samples CNS-10, the yield almost doubled, reaching 23%. Interestingly, CNS-15 showed 48% LLA yield with 57% selectivity, and further increment of ammonium persulfate to 20% did not enhance the LLA selectivity. This shows that the CNS-15 is the optimum catalyst for the direct conversion of glucose to LLA. The performance of CNS catalysts was compared to the reported catalytic systems in the literature (Table S3). Indeed, a few catalysts showed higher LLA yield compared to CNS; however, they rely on toxic chemicals and tedious synthesis protocols, leaving secondary/trace contaminations. CNS presents significant advantages over these catalysts because of its metal-free nature, synthesis from earth-abundant elements, high functionalization degree, relatively cheap precursors, and possibilities of further optimization by chemical route. After the reaction, the solid residue was collected by centrifugation and washed several times using THF and reused for the dehydration of glucose. Unfortunately, the catalytic performance was significantly decreased (negligible) after recycling, which might be due to the formation of polymeric humus during the first dehydration reaction. Because both humus and CNS has a polymeric structure, they remain bounded via $\pi-\pi$ interactions, resulting in the blocking of active sites on CNS. To validate the presence of humus in recycled catalysts, FT-IR analysis was performed on recycled catalysts, which demonstrates diminishing of characteristics triazine ($C_3N_3$) ring bending vibration at 806 $cm^{-1}$, and new peaks associated with carbonaceous materials appeared (Figure S13a). Furthermore, Raman spectra of the recycled catalyst exhibited intense D and G bands attributed to the presence of polymeric carbonaceous materials from humus (Figure S13b).

**Plausible Mechanism.** According to the obtained results and the existing literature, the following mechanism can be proposed for the glucose to LLA reaction (Figure 6). The hydrothermal treatment of glucose can lead to several reactions, namely, (i) reversion reaction to form cellobiose and levoglucosan,[101] (ii) degradation polymerization reaction to form humus, (iii) glucose epimerization to form fructose and mannose, and (iv) dehydration of C6 to C5 HMF.[12,102] It should be noted that each C5−C6 component can either decompose or polymerize to produce humin. Thus, catalysts with minimum humin production are desirable. Previous studies suggest that the conversion of glucose to LLA proceeds through dehydration of glucose to HMF, followed by rehydration of HMF to form LLA.[103] The CNS catalysts can facilitate the conversion of glucose to LLA via synergistic catalysis because of the presence of sulfonic/sulfate groups working as Brønsted/Lewis acidic sites while the terminal/uncondensed $NH_2$ and secondary N's (C═N:−C) work as a Brønsted/Lewis base.[104,105] The first step of glucose conversion is the isomerization of glucose to fructose in the presence of the Brønsted/Lewis basic sites on the CN (Figure 6, step-1).[106] The observance of a small amount of fructose suggests that the conversion of glucose to LLA proceeds through the isomerization step.[107] This was further evinced by using fructose as the substrate, which also gave LLA as the main product (35%) (Table S2). Glucose exists in two tautomeric forms: (i) glucopyranose (99%) and (ii) open-chain (0.25%) structure. The open-chain structure participates in the isomerization to form fructose. Because of the continuous consumption of the open-chain state, the tautomeric equilibrium shifts toward the open-chain to sustain fructose supply. The formed fructose further transforms to HMF in the presence of sulfonate/sulfate groups acting as a Brønsted/Lewis acid (Figure 6, step-2).[108] The glucose to HMF transformation proceeds via the stepwise release of three water molecules and the formation of enol and keto tautomeric intermediates.[109] Ultimately, the rehydration/ring-opening reaction of HMF followed through the 2,5-dioxo-3-hexenal and 5,5-dihydroxypent-3-ene-2-one intermediate, leading to the release of formic acid and production of LLA (Figure 6, step-3).[110] The observed high LLA selectivity for the CNS is associated with its unique features, namely, (i) the presence of plenty of sulfonate/sulfate functional groups compared to S-GCN, (ii) the high water dispersibility arising from the surface functionalization, and (iii) the structure which facilitate the better adsorption−desorption of reactant products.

## CONCLUSIONS

A CN structure with an exceptional degree of functionalization with sulfate/sulfonates was originally synthesized by thermal condensation of dicyandiamide and ammonium persulfate, as a source of C−N structures and S-functionalities, respectively. This was achieved under a self-pressurized condition in a quartz ampoule. The ssNMR and XPS displayed that functionalization of the CN structure proceeds with the transformation of the $Csp^2$ to $Csp^3$ structure, while the overall structural features of CN remain preserved. Because of the presence of plenty of Brønsted/Lewis acid/base catalytic centers, CNS catalysts can promote the direct conversion of glucose to LLA under hydrothermal conditions. The catalyst synthesized by using 15 wt % of ammonium persulfate in the dicyandiamide precursor displayed optimum catalytic performance at 200 °C for glucose dehydration/hydration to produce


https://doi.org/10.1021/acssuschemeng.2c00309
ACS Sustainable Chem. Eng. XXXX, XXX, XXX−XXX

LLA (≈48% yield). The proposed approach in this study provides an opportunity to synthesize new carbon/CN and even organic−inorganic hybrid materials that will make a significant advancement in the field of catalysis.

## ■ ASSOCIATED CONTENT

### Supporting Information

The Supporting Information is available free of charge at https://pubs.acs.org/doi/10.1021/acssuschemeng.2c00309.

Experimental details (materials and characterization); synthesis, product analysis, XPS, FE-SEM, TEM, UV−Vis, VB-XPS, XRD, and Raman, zeta potential, average particle size of CN and CNS, and GC−MS spectra of the reaction products (PDF)

## ■ AUTHOR INFORMATION


### Corresponding Authors

**Jinguang Hu** − *Department of Chemical and Petroleum Engineering, University of Calgary, Calgary, Alberta T2N 1N4, Canada;* orcid.org/0000-0001-8033-7102; Email: jinguang.hu@ucalgary.ca

**Md Golam Kibria** − *Department of Chemical and Petroleum Engineering, University of Calgary, Calgary, Alberta T2N 1N4, Canada;* orcid.org/0000-0003-3105-5576; Email: md.kibria@ucalgary.ca

### Authors

**Pawan Kumar** − *Department of Chemical and Petroleum Engineering, University of Calgary, Calgary, Alberta T2N 1N4, Canada*

**Ali Shayesteh Zeraati** − *Department of Chemical and Petroleum Engineering, University of Calgary, Calgary, Alberta T2N 1N4, Canada*

**Soumyabrata Roy** − *Department of Materials Science and NanoEngineering, Rice University, Houston, Texas 77030, United States;* orcid.org/0000-0003-3540-1341

**Kristen A. Miller** − *Department of Materials Science and NanoEngineering, Rice University, Houston, Texas 77030, United States;* orcid.org/0000-0002-5694-3169

**Aiguo Wang** − *Department of Chemical and Petroleum Engineering, University of Calgary, Calgary, Alberta T2N 1N4, Canada*

**Lawrence B. Alemany** − *Department of Chemistry and Shared Equipment Authority, Rice University, Houston, Texas 77005, United States;* orcid.org/0000-0001-7451-1020

**Tareq A. Al-Attas** − *Department of Chemical and Petroleum Engineering, University of Calgary, Calgary, Alberta T2N 1N4, Canada;* orcid.org/0000-0003-4305-735X

**Dhwanil Trivedi** − *Department of Chemical and Petroleum Engineering, University of Calgary, Calgary, Alberta T2N 1N4, Canada*

**Pulickel M. Ajayan** − *Department of Materials Science and NanoEngineering, Rice University, Houston, Texas 77030, United States;* orcid.org/0000-0001-8323-7860

Complete contact information is available at: https://pubs.acs.org/10.1021/acssuschemeng.2c00309


### Author Contributions

P.K. conceived the research, performed the catalyst synthesis, characterization, the reactions, and wrote the manuscript. A.S.Z. participated in the synthesis and helped in the reaction setup, characterization, and product analysis. S.R. performed the XPS and Raman analysis. K.M. performed the TEM analysis. A.W. performed the HPLC analysis of the reaction products. L.A. performed the ssNMR analysis and wrote the discussion. L.A. also contributed to the XPS analysis. T.A.A. helped in the characterization of products. P.A., J.H., and M.G.K. supervised the research and edited the manuscript. All co-authors read and approved the final version of the manuscript. P.K. and A.S.Z. contributed equally.

### Notes

The authors declare no competing financial interest.

## ■ ACKNOWLEDGMENTS

The authors would like to thank the Department of Chemical and Petroleum Engineering in the Schulich School of Engineering and the University of Calgary CFREF fund for financial assistance. The authors are also thankful to Dr. Wade White and Ms. Bruna Palma for the GC−MS analysis of the samples. Dr. Maryam Razi and Prof. Edward Robert are acknowledged to allow access of DLS through the CPE RITS scheme. The authors acknowledge Dr. Zhaofei Li and Prof. Hua Song for $NH_3$-TPD and TGA-DSC analyses.

## ■ REFERENCES


(1) Liu, Y.; Nie, Y.; Lu, X.; Zhang, X.; He, H.; Pan, F.; Zhou, L.; Liu, X.; Ji, X.; Zhang, S. Cascade Utilization of Lignocellulosic Biomass to High-value Products. *Green Chem.* **2019**, *21*, 3499−3535.

(2) Thomas, B.; Raj, M. C.; Joy, J.; Moores, A.; Drisko, G. L.; Sanchez, C. Nanocellulose, A Versatile Green Platform: From Biosources to Materials and Their Applications. *Chem. Rev.* **2018**, *118*, 11575−11625.

(3) Holladay, J. E.; White, J. F.; Bozell, J. J.; Johnson, D. *Top Value-Added Chemicals From Biomass-Volume II—Results of Screening for Potential Candidates from Biorefinery Lignin*; Pacific Northwest National Lab. (PNNL): Richland, WA (United States), 2007

(4) Hayes, G. C.; Becer, C. R. Levulinic acid: A sustainable platform chemical for novel polymer architectures. *Polym. Chem.* **2020**, *11*, 4068−4077.

(5) Pileidis, F. D.; Titirici, M. M. Levulinic acid biorefineries: new challenges for efficient utilization of biomass. *ChemSusChem* **2016**, *9*, 562−582.

(6) Yan, K.; Jarvis, C.; Gu, J.; Yan, Y. Production and catalytic transformation of levulinic acid: A platform for speciality chemicals and fuels. *Renewable Sustainable Energy Rev.* **2015**, *51*, 986−997.

(7) Global Levulinic Acid Market Research Report 2020 Publisher: QY Research, Published on 02/01/2020 https://www.researchandmarkets.com/reports/5353362/levulinic-acid-market-global-industry-trends. Date of access: April 26, 2022.

(8) Bozell, J. J.; Moens, L.; Elliott, D.; Wang, Y.; Neuenscwander, G.; Fitzpatrick, S.; Bilski, R.; Jarnefeld, J. Production of levulinic acid and use as a platform chemical for derived products. *Resour., Conserv. Recycl.* **2000**, *28*, 227−239.

(9) Meramo-Hurtado, S. I.; Ojeda, K. A.; Sanchez-Tuiran, E. Environmental and safety assessments of industrial production of levulinic acid via acid-catalyzed dehydration. *ACS Omega* **2019**, *4*, 22302−22312.

(10) Kang, S.; Zhang, G.; Yang, X.; Yin, H.; Fu, X.; Liao, J.; Tu, J.; Huang, X.; Qin, F. G.; Xu, Y. Effects of p-toluenesulfonic acid in the conversion of glucose for levulinic acid and sulfonated carbon production. *Energy Fuels* **2017**, *31*, 2847−2854.

(11) Badgujar, K. C.; Wilson, L. D.; Bhanage, B. M. Recent advances for sustainable production of levulinic acid in ionic liquids from biomass: Current scenario, opportunities and challenges. *Renewable Sustainable Energy Rev.* **2019**, *102*, 266−284.

(12) Weingarten, R.; Kim, Y. T.; Tompsett, G. A.; Fernández, A.; Han, K. S.; Hagaman, E. W.; Conner, W. C., Jr.; Dumesic, J. A.;

Huber, G. W. Conversion of glucose into levulinic acid with solid metal (IV) phosphate catalysts. *J. Catal.* **2013**, *304*, 123−134.
(13) Pyo, S.-H.; Glaser, S. J.; Rehnberg, N.; Hatti-Kaul, R. Clean production of levulinic acid from fructose and glucose in salt water by heterogeneous catalytic dehydration. *ACS Omega* **2020**, *5*, 14275−14282.
(14) Qu, Y.; Zhao, Y.; Xiong, S.; Wang, C.; Wang, S.; Zhu, L.; Ma, L. Conversion of glucose into 5-hydroxymethylfurfural and levulinic acid catalyzed by $SO_4^{2-}/ZrO_2$ in a biphasic solvent system. *Energy Fuels* **2020**, *34*, 11041−11049.
(15) Liu, X.; Zhou, Y.; Zhou, W.; Li, L.; Huang, S.; Chen, S. Biomass-derived nitrogen self-doped porous carbon as effective metal-free catalysts for oxygen reduction reaction. *Nanoscale* **2015**, *7*, 6136−6142.
(16) Wen, G.; Gu, Q.; Liu, Y.; Schlögl, R.; Wang, C.; Tian, Z.; Su, D. S. Biomass-Derived Graphene-like Carbon: Efficient Metal-Free Carbocatalysts for Epoxidation. *Angew. Chem., Int. Ed.* **2018**, *57*, 16898−16902.
(17) Barrio, J.; Volokh, M.; Shalom, M. Polymeric carbon nitrides and related metal-free materials for energy and environmental applications. *J. Mater. Chem. A* **2020**, *8*, 11075−11116.
(18) Kumar, P.; Laishram, D.; Sharma, R. K.; Vinu, A.; Hu, J.; Kibria, M. G. Boosting Photocatalytic Activity Using Carbon Nitride Based 2D/2D van der Waals Heterojunctions. *Chem. Mater.* **2021**, *33*, 9012−9092.
(19) Thomas, A.; Fischer, A.; Goettmann, F.; Antonietti, M.; Müller, J.-O.; Schlögl, R.; Carlsson, J. M. Graphitic carbon nitride materials: variation of structure and morphology and their use as metal-free catalysts. *J. Mater. Chem.* **2008**, *18*, 4893−4908.
(20) Talapaneni, S. N.; Singh, G.; Kim, I. Y.; AlBahily, K.; Al-Muhtaseb, A. A. H.; Karakoti, A. S.; Tavakkoli, E.; Vinu, A. Nanostructured carbon nitrides for $CO_2$ capture and conversion. *Adv. Mater.* **2020**, *32*, No. 1904635.
(21) Yang, Z.; Zhang, Y.; Schnepp, Z. Soft and hard templating of graphitic carbon nitride. *J. Mater. Chem. A* **2015**, *3*, 14081−14092.
(22) Chauhan, D. K.; Jain, S.; Battula, V. R.; Kailasam, K. Organic motif's functionalization via covalent linkage in carbon nitride: An exemplification in photocatalysis. *Carbon* **2019**, *152*, 40−58.
(23) Gong, X.; Yu, S.; Guan, M.; Zhu, X.; Xue, C. Pyrene-functionalized polymeric carbon nitride with promoted aqueous−organic biphasic photocatalytic $CO_2$ reduction. *J. Mater. Chem. A* **2019**, *7*, 7373−7379.
(24) de Almeida Ribeiro, R. S.; Monteiro Ferreira, L. E.; Rossa, V.; Lima, C. G.; Paixão, M. W.; Varma, R. S.; de Melo Lima, T. Graphitic carbon nitride-based materials as catalysts for the upgrading of lignocellulosic biomass-derived molecules. *ChemSusChem* **2020**, *13*, 3992−4004.
(25) Kumar, S.; Gawande, M. B.; Kopp, J.; Kment, S.; Varma, R. S.; Zbořil, R. P-and F-co-doped carbon nitride nanocatalysts for photocatalytic $CO_2$ reduction and thermocatalytic furanics synthesis from sugars. *ChemSusChem* **2020**, *13*, 5231−5238.
(26) Wang, J.; Kumar, P.; Zhao, H.; Kibria, M. G.; Hu, J. Polymeric carbon nitride-based photocatalysts for photoreforming of biomass derivatives. *Green Chem.* **2021**, *23*, 7435−7457.
(27) Baig, R. N.; Verma, S.; Nadagouda, M. N.; Varma, R. Room temperature synthesis of biodiesel using sulfonated graphitic carbon nitride. *Sci. Rep.* **2016**, *6*, 39387.
(28) Verma, S.; Baig, R. N.; Nadagouda, M. N.; Len, C.; Varma, R. S. Sustainable pathway to furanics from biomass via heterogeneous organo-catalysis. *Green Chem.* **2017**, *19*, 164−168.
(29) Chhabra, T.; Bahuguna, A.; Dhankhar, S. S.; Nagaraja, C.; Krishnan, V. Sulfonated graphitic carbon nitride as a highly selective and efficient heterogeneous catalyst for the conversion of biomass-derived saccharides to 5-hydroxymethylfurfural in green solvents. *Green Chem.* **2019**, *21*, 6012−6026.
(30) Acharya, S.; Martha, S.; Sahoo, P. C.; Parida, K. Glimpses of the modification of perovskite with graphene-analogous materials in photocatalytic applications. *Inorg. Chem. Front.* **2015**, *2*, 807−823.
(31) Qin, L.; Ishizaki, T.; Takeuchi, N.; Takahashi, K.; Kim, K. H.; Li, O. L. Green Sulfonation of Carbon Catalysts via Gas−Liquid Interfacial Plasma for Cellulose Hydrolysis. *ACS Sustainable Chem. Eng.* **2020**, *8*, 5837−5846.
(32) Liu, Y.; Liu, L.; Wang, K.; Zhang, H.; Yuan, Y.; Wei, H.; Wang, X.; Duan, Y.; Zhou, L.; Zhang, J. Modified ammonium persulfate oxidations for efficient preparation of carboxylated cellulose nanocrystals. *Carbohydr. Polym.* **2020**, *229*, No. 115572.
(33) Xia, X.; Zhu, F.; Li, J.; Yang, H.; Wei, L.; Li, Q.; Jiang, J.; Zhang, G.; Zhao, Q. A review study on sulfate-radical-based advanced oxidation processes for domestic/industrial wastewater treatment: degradation, efficiency, and mechanism. *Front. Chem.* **2020**, *8*, No. 592056.
(34) Zhang, Y.; Mori, T.; Ye, J.; Antonietti, M. Phosphorus-doped carbon nitride solid: enhanced electrical conductivity and photocurrent generation. *J. Am. Chem. Soc.* **2010**, *132*, 6294−6295.
(35) Kumar, P.; Kar, P.; Manuel, A. P.; Zeng, S.; Thakur, U. K.; Alam, K. M.; Zhang, Y.; Kisslinger, R.; Cui, K.; Bernard, G. M.; Michaelis, V. K.; Shankar, K. Noble metal free, visible light driven photocatalysis using $TiO_2$ nanotube arrays sensitized by P-foped $C_3N_4$ quantum dots. *Adv. Opt. Mater.* **2020**, *8*, No. 1901275.
(36) Noda, Y.; Merschjann, C.; Tarábek, J.; Amsalem, P.; Koch, N.; Bojdys, M. J. Directional Charge Transport in Layered Two-Dimensional Triazine-Based Graphitic Carbon Nitride. *Angew. Chem.* **2019**, *131*, 9494−9498.
(37) Lin, L.; Yu, Z.; Wang, X. Crystalline carbon nitride semiconductors for photocatalytic water splitting. *Angew. Chem.* **2019**, *131*, 6225−6236.
(38) Jürgens, B.; Irran, E.; Senker, J.; Kroll, P.; Müller, H.; Schnick, W. Melem (2, 5, 8-triamino-tri-s-triazine), an important intermediate during condensation of melamine rings to graphitic carbon nitride: Synthesis, structure determination by X-ray powder diffractometry, solid-state NMR, and theoretical studies. *J. Am. Chem. Soc.* **2003**, *125*, 10288−10300.
(39) Lotsch, B. V.; Döblinger, M.; Sehnert, J.; Seyfarth, L.; Senker, J.; Oeckler, O.; Schnick, W. Unmasking melon by a complementary approach employing electron diffraction, solid-state NMR spectroscopy, and theoretical calculations—structural characterization of a carbon nitride polymer. *Chem. − Eur. J.* **2007**, *13*, 4969−4980.
(40) Seyfarth, L.; Senker, J. An NMR crystallographic approach for the determination of the hydrogen substructure of nitrogen bonded protons. *Phys. Chem. Chem. Phys.* **2009**, *11*, 3522−3531.
(41) Seyfarth, L.; Seyfarth, J.; Lotsch, B. V.; Schnick, W.; Senker, J. Tackling the stacking disorder of melon—structure elucidation in a semicrystalline material. *Phys. Chem. Chem. Phys.* **2010**, *12*, 2227−2237.
(42) Hu, Y.; Shim, Y.; Oh, J.; Park, S.; Park, S.; Ishii, Y. Synthesis of 13C-, 15N-labeled graphitic carbon nitrides and NMR-based evidence of hydrogen-bonding assisted two-dimensional assembly. *Chem. Mater.* **2017**, *29*, 5080−5089.
(43) Li, X.; Sergeyev, I. V.; Aussenac, F.; Masters, A. F.; Maschmeyer, T.; Hook, J. M. Dynamic nuclear polarization NMR spectroscopy of polymeric carbon nitride photocatalysts: insights into structural defects and reactivity. *Angew. Chem.* **2018**, *130*, 6964−6968.
(44) Liu, G.; Niu, P.; Sun, C.; Smith, S. C.; Chen, Z.; Lu, G. Q.; Cheng, H.-M. Unique electronic structure induced high photoreactivity of sulfur-doped graphitic $C_3N_4$. *J. Am. Chem. Soc.* **2010**, *132*, 11642−11648.
(45) Ge, L.; Han, C.; Xiao, X.; Guo, L.; Li, Y. Enhanced visible light photocatalytic hydrogen evolution of sulfur-doped polymeric g-$C_3N_4$ photocatalysts. *Mater. Res. Bull.* **2013**, *48*, 3919−3925.
(46) Feng, L.-L.; Zou, Y.; Li, C.; Gao, S.; Zhou, L.-J.; Sun, Q.; Fan, M.; Wang, H.; Wang, D.; Li, G.-D. Nanoporous sulfur-doped graphitic carbon nitride microrods: a durable catalyst for visible-light-driven $H_2$ evolution. *Int. J. Hydrogen Energy* **2014**, *39*, 15373−15379.
(47) Jourshabani, M.; Shariatinia, Z.; Badiei, A. Controllable synthesis of mesoporous sulfur-doped carbon nitride materials for


https://doi.org/10.1021/acssuschemeng.2c00309
ACS Sustainable Chem. Eng. XXXX, XXX, XXX−XXX

enhanced visible light photocatalytic degradation. *Langmuir* **2017**, *33*, 7062−7078.
(48) Wang, H.; Bian, Y.; Hu, J.; Dai, L. Highly crystalline sulfur-doped carbon nitride as photocatalyst for efficient visible-light hydrogen generation. *Appl. Catal., B* **2018**, *238*, 592−598.
(49) Li, D.; Chung, Y. W.; Yang, S.; Wong, M. S.; Adibi, F.; Sproul, W. D. Infrared absorption and nuclear magnetic resonance studies of carbon nitride thin films prepared by reactive magnetron sputtering. *J. Vac. Sci. Technol., A* **1994**, *12*, 1470−1473.
(50) Sanchez-Lopez, J.; Donnet, C.; Lefebvre, F.; Fernandez-Ramos, C.; Fernandez, A. Bonding structure in amorphous carbon nitride: a spectroscopic and nuclear magnetic resonance study. *J. Appl. Phys.* **2001**, *90*, 675−681.
(51) Gammon, W.; Hoatson, G.; Holloway, B.; Vold, R.; Reilly, A. Bonding in hard and elastic amorphous carbon nitride films investigated using $^{15}N$, $^{13}C$, and $^{1}H$ NMR spectroscopy. *Phys. Rev. B* **2003**, *68*, No. 195401.
(52) Lau, V. W.-H.; Mesch, M. B.; Duppel, V.; Blum, V.; Senker, J. R.; Lotsch, B. V. Low-molecular-weight carbon nitrides for solar hydrogen evolution. *J. Am. Chem. Soc.* **2015**, *137*, 1064−1072.
(53) Erdogan, D. A.; Sevim, M.; Kısa, E.; Emiroglu, D. B.; Karatok, M.; Vovk, E. I.; Bjerring, M.; Akbey, Ü.; Metin, Ö.; Ozensoy, E. Photocatalytic activity of mesoporous graphitic carbon nitride (mpg-$C_3N_4$) towards organic chromophores under UV and VIS light illumination. *Top. Catal.* **2016**, *59*, 1305−1318.
(54) Xiao-jing, Y.; Bing-wen, H. Probing $^{15}N$-$^{15}N$ Correlations in $gC_3N_4$ Samples with Solid-State NMR SHA$^+$ Pulse Sequence. *Chin. J. Magn. Reson.* **2016**, *33*, 361−367.
(55) Wang, X. L.; Fang, W. Q.; Liu, W.; Jia, Y.; Jing, D.; Wang, Y.; Yang, L.-Y.; Gong, X.-Q.; Yao, Y.-F.; Yang, H. G. Brønsted base site engineering of graphitic carbon nitride for enhanced photocatalytic activity. *J. Mater. Chem. A* **2017**, *5*, 19227−19236.
(56) Wang, Y.; Zhang, Y.; Zhao, S.; Huang, Z.; Chen, W.; Zhou, Y.; Lv, X.; Yuan, S. Bio-template synthesis of Mo-doped polymer carbon nitride for photocatalytic hydrogen evolution. *Appl. Catal., B* **2019**, *248*, 44−53.
(57) Damodaran, K.; Sanjayan, G. J.; Rajamohanan, P. R.; Ganapathy, S.; Ganesh, K. N. Solid state NMR of a molecular self-assembly: multinuclear approach to the cyanuric acid-melamine system. *Org. Lett.* **2001**, *3*, 1921−1924.
(58) Lotsch, B. V.; Schnick, W. New light on an old story: formation of melam during thermal condensation of melamine. *Chem. − Eur. J.* **2007**, *13*, 4956−4968.
(59) Lotsch, B. V.; Schnick, W. From triazines to heptazines: novel nonmetal tricyanomelaminates as precursors for graphitic carbon nitride materials. *Chem. Mater.* **2006**, *18*, 1891−1900.
(60) Sattler, A.; Seyfarth, L.; Senker, J.; Schnick, W. Synthesen, Kristallstrukturen und spektroskopische Eigenschaften des Melem-Adduktes $C_6N_7(NH_2)_3{\cdot}H_3PO_4$ sowie der Melemium-Salze $(H_2C_6N_7(NH_2)_3)SO_4{\cdot}2H_2O$ und $(HC_6N_7(NH_2)_3)ClO_4{\cdot}$ $H_2O$. *Z. Anorg. Allg. Chem.* **2005**, *631*, 2545−2554.
(61) Saplinova, T.; Bakumov, V.; Gmeiner, T.; Wagler, J.; Schwarz, M.; Kroke, E. 2, 5, 8-Trihydrazino-s-heptazine: A Precursor for Heptazine-based Iminophosphoranes. *Z. Anorg. Allg. Chem.* **2009**, *635*, 2480−2487.
(62) Sattler, A.; Pagano, S.; Zeuner, M.; Zurawski, A.; Gunzelmann, D.; Senker, J.; Müller-Buschbaum, K.; Schnick, W. Melamine−melem adduct phases: investigating the thermal condensation of melamine. *Chem. − Eur. J.* **2009**, *15*, 13161−13170.
(63) Makowski, S. J.; Köstler, P.; Schnick, W. Formation of a Hydrogen-Bonded Heptazine Framework by Self-Assembly of Melem into a Hexagonal Channel Structure. *Chem. − Eur. J.* **2012**, *18*, 3248−3257.
(64) El-Gamel, N. E.; Seyfarth, L.; Wagler, J.; Ehrenberg, H.; Schwarz, M.; Senker, J.; Kroke, E. The tautomeric forms of cyameluric acid derivatives. *Chem. − Eur. J.* **2007**, *13*, 1158−1173.
(65) Seyfarth, L.; Sehnert, J.; El-Gamel, N.; Milius, W.; Kroke, E.; Breu, J.; Senker, J. Structure elucidation of cyameluric acid by combining solid-state NMR spectroscopy, molecular modeling and direct-space methods. *J. Mol. Struct.* **2008**, *889*, 217−228.
(66) Schlomberg, H.; Kröger, J.; Savasci, G. K.; Terban, M. W.; Bette, S.; Moudrakovski, I.; Duppel, V.; Podjaski, F.; Siegel, R.; Senker, J. R. Structural insights into poly (heptazine imides): a light-storing carbon nitride material for dark photocatalysis. *Chem. Mater.* **2019**, *31*, 7478−7486.
(67) Lau, V. W.-H.; Moudrakovski, I.; Botari, T.; Weinberger, S.; Mesch, M. B.; Duppel, V.; Senker, J.; Blum, V.; Lotsch, B. V. Rational design of carbon nitride photocatalysts by identification of cyanamide defects as catalytically relevant sites. *Nat. Commun.* **2016**, *7*, 12165.
(68) Bonhomme, C.; Babonneau, F.; Maquet, J.; Livage, J.; Vaultier, M.; Framery, E. Studies of model organic and inorganic compounds by $^{15}N$ CP MAS NMR using Inversion Recovery Cross Polarization. *J. Chim. Phys.* **1995**, *92*, 1881−1884.
(69) Gervais, C.; Babonneau, F.; Maquet, J.; Bonhomme, C.; Massiot, D.; Framery, E.; Vaultier, M. $^{15}N$ cross-polarization using the inversion−recovery cross-polarization technique and $^{11}B$ magic angle spinning NMR studies of reference compounds containing B-N bonds. *Mag. Reson. Chem.* **1998**, *36*, 407−414.
(70) Gervais, C.; Maquet, J.; Babonneau, F.; Duriez, C.; Framery, E.; Vaultier, M.; Florian, P.; Massiot, D. Chemically derived BN ceramics: Extensive $^{11}B$ and $^{15}N$ solid-state NMR study of a preceramic polyborazilene. *Chem. Mater.* **2001**, *13*, 1700−1707.
(71) Sangill, R.; Rastrupandersen, N.; Bildsoe, H.; Jakobsen, H.; Nielsen, N. Optimized spectral editing of $^{13}C$ MAS NMR spectra of rigid solids using cross-polarization methods. *J. Magn. Reson., Ser. A* **1994**, *107*, 67−78.
(72) Zhou, C.; Zeng, Z.; Zeng, G.; Huang, D.; Xiao, R.; Cheng, M.; Zhang, C.; Xiong, W.; Lai, C.; Yang, Y. Visible-light-driven photocatalytic degradation of sulfamethazine by surface engineering of carbon nitride: Properties, degradation pathway and mechanisms. *J. Hazard. Mater.* **2019**, *380*, No. 120815.
(73) Wu, Y.; Wen, M.; Navlani-García, M.; Kuwahara, Y.; Mori, K.; Yamashita, H. Palladium nanoparticles supported on titanium-doped graphitic carbon nitride for formic acid dehydrogenation. *Chem. − Asian J.* **2017**, *12*, 860−867.
(74) Tian, H.; Liu, M.; Zheng, W. Constructing 2D graphitic carbon nitride nanosheets/layered $MoS_2$/graphene ternary nanojunction with enhanced photocatalytic activity. *Appl. Catal., B* **2018**, *225*, 468−476.
(75) Zhang, Y.; Park, S.-J. Stabilizing CuPd bimetallic alloy nanoparticles deposited on holey carbon nitride for selective hydroxylation of benzene to phenol. *J. Catal.* **2019**, *379*, 154−163.
(76) Na, S.; Minhua, Z.; Xiuqin, D.; Lingtao, W. Preparation of sulfonated ordered mesoporous carbon catalyst and its catalytic performance for esterification of free fatty acids in waste cooking oils. *RSC Adv.* **2019**, *9*, 15941−15948.
(77) Katsyuba, S.; Kovalenko, V.; Chernova, A.; Vandyukova, E.; Zverev, V.; Shagidullin, R.; Antipin, I.; Solovieva, S.; Stoikov, I.; Konovalov, A. Vibrational spectra, co-operative intramolecular hydrogen bonding and conformations of calix [4] arene and thiacalix [4] arene molecules and their para-tert-butyl derivatives. *Org. Biomol. Chem.* **2005**, *3*, 2558−2565.
(78) Tan, H.; Gu, X.; Kong, P.; Lian, Z.; Li, B.; Zheng, Z. Cyano group modified carbon nitride with enhanced photoactivity for selective oxidation of benzylamine. *Appl. Catal., B* **2019**, *242*, 67−75.
(79) Xia, P.; Antonietti, M.; Zhu, B.; Heil, T.; Yu, J.; Cao, S. Designing defective crystalline carbon nitride to enable selective $CO_2$ photoreduction in the gas phase. *Adv. Funct. Mater.* **2019**, *29*, No. 1900093.
(80) Guo, H.; Liu, Y.; Ma, W.; Yan, L.; Li, K.; Lin, S. Surface molecular imprinting on carbon microspheres for fast and selective adsorption of perfluorooctane sulfonate. *J. Hazard. Mater.* **2018**, *348*, 29−38.
(81) Zhang, J.; Teng, H.; Bin, L.; Lin, L.; Zelun, Z.; Daqiang, H.; Xiaohua, J.; Guotao, W.; Ping, C. Effects of graphitic carbon nitride on the dehydrogenation of ammonia borane. *Chin. J. Catal.* **2013**, *34*, 1303−1311.


https://doi.org/10.1021/acssuschemeng.2c00309
ACS Sustainable Chem. Eng. XXXX, XXX, XXX−XXX

(82) Ran, Y.; Yu, X.; Liu, J.; Cui, J.; Wang, J.; Wang, L.; Zhang, Y.; Xiang, X.; Ye, J. Polymeric carbon nitride with frustrated Lewis pair sites for enhanced photofixation of nitrogen. *J. Mater. Chem. A* **2020**, *8*, 13292−13298.
(83) Choudhary, P.; Sen, A.; Kumar, A.; Dhingra, S.; Nagaraja, C.; Krishnan, V. Sulfonic acid functionalized graphitic carbon nitride as solid acid−base bifunctional catalyst for Knoevenagel condensation and multicomponent tandem reactions. *Mater. Chem. Front.* **2021**, *5*, 6265−6278.
(84) Wang, G.; Zhang, T.; Yu, W.; Si, R.; Liu, Y.; Zhao, Z. Modulating location of single copper atoms in polymeric carbon nitride for enhanced photoredox catalysis. *ACS Catal.* **2020**, *10*, 5715−5722.
(85) Xie, Y.; Li, Y.; Huang, Z.; Zhang, J.; Jia, X.; Wang, X.-S.; Ye, J. Two types of cooperative nitrogen vacancies in polymeric carbon nitride for efficient solar-driven $H_2O_2$ evolution. *Appl. Catal., B* **2020**, *265*, No. 118581.
(86) Zhao, C.; Li, Q.; Xie, Y.; Zhang, L.; Xiao, X.; Wang, D.; Jiao, Y.; Price, C. A. H.; Jiang, B.; Liu, J. Three-dimensional assemblies of carbon nitride tubes as nanoreactors for enhanced photocatalytic hydrogen production. *J. Mater. Chem. A* **2020**, *8*, 305−312.
(87) Zhang, M.; Zhu, K.; Qin, L.; Kang, S.-Z.; Li, X. Enhanced electron transfer and photocatalytic hydrogen production over the carbon nitride/porphyrin nanohybrid finely bridged by special copper. *Catal. Sci. Technol.* **2020**, *10*, 1640−1649.
(88) Lin, K.-Y. A.; Yang, M.-T.; Zhang, Z.-Y.; Wi-Afedzi, T.; Lin, Y.-F. Prussian Blue analogue supported on sulfur-doped carbon nitride as an enhanced heterogeneous catalyst for activating peroxymonosulfate. *J. Colloid Interface Sci.* **2018**, *529*, 161−170.
(89) Shayesteh Zeraati, A.; Sharif, F.; Aliabadian, E.; Roberts, E. P.; Sundararaj, U. Co-Doped Electrochemically Exfoliated Graphene/Polymer Nanocomposites with High Dielectric Constant and Low Dielectric Loss for Flexible Dielectrics and Charge Storage. *ACS Appl. Nano Mater.* **2020**, *3*, 4512−4521.
(90) Razzaq, A. A.; Yao, Y.; Shah, R.; Qi, P.; Miao, L.; Chen, M.; Zhao, X.; Peng, Y.; Deng, Z. High-performance lithium sulfur batteries enabled by a synergy between sulfur and carbon nanotubes. *Energy Storage Mater.* **2019**, *16*, 194−202.
(91) Zhang, Q.; Liu, Y.; Nie, Y.; Liu, Y.; Ma, Q. Wavelength-Dependent surface plasmon coupling electrochemiluminescence biosensor based on Sulfur-Doped carbon nitride quantum dots for K-RAS gene detection. *Anal. Chem.* **2019**, *91*, 13780−13786.
(92) Wu, Y.; Wang, H.; Tu, W.; Wu, S.; Liu, Y.; Tan, Y. Z.; Luo, H.; Yuan, X.; Chew, J. W. Petal-like CdS nanostructures coated with exfoliated sulfur-doped carbon nitride via chemically activated chain termination for enhanced visible-light−driven photocatalytic water purification and $H_2$ generation. *Appl. Catal., B* **2018**, *229*, 181−191.
(93) Wang, H.; Qiu, X.; Wang, W.; Jiang, L.; Liu, H. Iron sulfide nanoparticles embedded into a nitrogen and sulfur co-doped carbon sphere as a highly active oxygen reduction electrocatalyst. *Front. Chem.* **2019**, *7*, 855.
(94) Xu, C.; Han, Q.; Zhao, Y.; Wang, L.; Li, Y.; Qu, L. Sulfur-doped graphitic carbon nitride decorated with graphene quantum dots for an efficient metal-free electrocatalyst. *J. Mater. Chem. A* **2015**, *3*, 1841−1846.
(95) Wang, K.; Li, Q.; Liu, B.; Cheng, B.; Ho, W.; Yu, J. Sulfur-doped g-$C_3N_4$ with enhanced photocatalytic $CO_2$-reduction performance. *Appl. Catal., B* **2015**, *176-177*, 44−52.
(96) Maerten, S.; Kumpidet, C.; Voß, D.; Bukowski, A.; Wasserscheid, P.; Albert, J. Glucose oxidation to formic acid and methyl formate in perfect selectivity. *Green Chem.* **2020**, *22*, 4311−4320.
(97) Baldi, G.; Goto, S.; Chow, C.-K.; Smith, J. Catalytic Oxidation of Formic Acid in Water. Intraparticle Diffusion in Liquid-Filled Pores. *Ind. Eng. Chem. Process Des. Dev.* **1974**, *13*, 447−452.
(98) Kabyemela, B. M.; Adschiri, T.; Malaluan, R. M.; Arai, K.; Ohzeki, H. Rapid and selective conversion of glucose to erythrose in supercritical water. *Ind. Eng. Chem. Res.* **1997**, *36*, 5063−5067.
(99) Song, J.; Fan, H.; Ma, J.; Han, B. Conversion of glucose and cellulose into value-added products in water and ionic liquids. *Green Chem.* **2013**, *15*, 2619−2635.
(100) Yang, F.; Zhang, S.; Cheng, K.; Antonietti, M. A hydrothermal process to turn waste biomass into artificial fulvic and humic acids for soil remediation. *Sci. Total Environ.* **2019**, *686*, 1140−1151.
(101) Van Dam, H.; Kieboom, A.; Van Bekkum, H. The conversion of fructose and glucose in acidic media: formation of hydroxymethylfurfural. *Starch* **1986**, *38*, 95−101.
(102) Kumar, K.; Parveen, F.; Patra, T.; Upadhyayula, S. Hydrothermal conversion of glucose to levulinic acid using multifunctional ionic liquids: effects of metal ion co-catalysts on the product yield. *New J. Chem.* **2018**, *42*, 228−236.
(103) Qu, H.; Liu, B.; Gao, G.; Ma, Y.; Zhou, Y.; Zhou, H.; Li, L.; Li, Y.; Liu, S. Metal-organic framework containing Brønsted acidity and Lewis acidity for efficient conversion glucose to levulinic acid. *Fuel Process. Technol.* **2019**, *193*, 1−6.
(104) Weingarten, R.; Cho, J.; Xing, R.; Conner, W. C., Jr.; Huber, G. W. Kinetics and reaction engineering of levulinic acid production from aqueous glucose solutions. *ChemSusChem* **2012**, *5*, 1280−1290.
(105) Girisuta, B.; Dussan, K.; Haverty, D.; Leahy, J.; Hayes, M. A kinetic study of acid catalysed hydrolysis of sugar cane bagasse to levulinic acid. *Chem. Eng. J.* **2013**, *217*, 61−70.
(106) Chen, S. S.; Yu, I. K.; Cho, D.-W.; Song, H.; Tsang, D. C.; Tessonnier, J.-P.; Ok, Y. S.; Poon, C. S. Selective glucose isomerization to fructose via a nitrogen-doped solid base catalyst derived from spent coffee grounds. *ACS Sustainable Chem. Eng.* **2018**, *6*, 16113−16120.
(107) Choudhary, V.; Mushrif, S. H.; Ho, C.; Anderko, A.; Nikolakis, V.; Marinkovic, N. S.; Frenkel, A. I.; Sandler, S. I.; Vlachos, D. G. Insights into the interplay of Lewis and Brønsted acid catalysts in glucose and fructose conversion to 5-(hydroxymethyl) furfural and levulinic acid in aqueous media. *J. Am. Chem. Soc.* **2013**, *135*, 3997−4006.
(108) Körner, P.; Jung, D.; Kruse, A. The effect of different Brønsted acids on the hydrothermal conversion of fructose to HMF. *Green Chem.* **2018**, *20*, 2231−2241.
(109) Weingarten, R.; Conner, W. C.; Huber, G. W. Production of Levulinic Acid from Cellulose by Hydrothermal Decomposition Combined with Aqueous Phase Dehydration with A Solid Acid catalyst. *Energy Environ. Sci.* **2012**, *5*, 7559−7574.
(110) Peng, L.; Lin, L.; Zhang, J.; Zhuang, J.; Zhang, B.; Gong, Y. Catalytic Conversion of Cellulose to Levulinic Acid by Metal Chlorides. *Molecules* **2010**, *15*, 5258−5272.


https://doi.org/10.1021/acssuschemeng.2c00309
*ACS Sustainable Chem. Eng.* XXXX, XXX, XXX−XXX